

Portable, Massively Parallel Implementation of a Material Point Method for Compressible Flows

Paolo Joseph Baioni⁽¹⁾, Tommaso Benacchio⁽²⁾,
Luigi Capone⁽³⁾, Carlo de Falco⁽¹⁾

April 29, 2024

⁽¹⁾ MOX – Modelling and Scientific Computing
Dipartimento di Matematica, Politecnico di Milano
Piazza Leonardo da Vinci 32, 20133 Milano, Italy
`{paolojoseph.baioni,carlo.defalco}@polimi.it`

⁽²⁾ Danish Meteorological Institute
Sankt Kjelds Plads 11
2100 Copenhagen, Denmark
`tbo@dmi.dk`

⁽³⁾ Leonardo Labs, Leonardo S.p.A.
Torre Fiumara, Via Raffaele Pieragostini, 80, 16149 Genova, Italy
`luigi.capone@leonardo.com`

Keywords: Material Point Method; GPUs; Supersonic Gas Dynamics;
Performance Portability; High-Performance Computing.

This work has not yet been peer-reviewed and is provided by the contributing authors as a means to ensure timely dissemination of scholarly and technical work on a non-commercial basis. Copyright and all rights therein are maintained by the authors or by other copyright owners. It is understood that all persons copying this information will adhere to the terms and constraints invoked by each author's copyright. This work may not be reposted without explicit permission of the copyright owner. This work has been submitted for publication. Copyright in this work may be transferred without further notice.

Abstract

The recent evolution of software and hardware technologies is leading to a renewed computational interest in Particle-In-Cell (PIC) methods such as the Material Point Method (MPM). Indeed, provided some critical aspects are properly handled, PIC methods can be cast in formulations suitable to the requirements of data locality and fine-grained parallelism of modern hardware accelerators as Graphics Processing Units (GPUs). Such a rapid and continuous technological development increases also the importance of generic and portable implementations. While continuum mechanics simulations have already shown the capabilities of MPM on a wide range of phenomena, the use of the method in compressible fluid dynamics is less frequent, especially in the supersonic regime.

In this paper we present a portable, highly parallel, GPU based MPM solver for compressible gas dynamics. The implementation aims to reach a good compromise between portability and efficiency and to give a first assessment of the potential of this approach in reproducing high speed gas flows, also taking into account solid obstacles. The proposed model constitutes a new step towards the realization of a monolithic MPM solver for Fluid-Structure Interaction (FSI) problems at all Mach numbers up to the supersonic regime.

1 Introduction and Motivation

Hardware and software technology evolution has led to a renewed interest in particle-based numerical techniques for differential problems, such as the Material Point Method (MPM, [45, 56]), that was developed stemming from the Particle In Cell method *Fluid Implicit Particle Method* [26, 7] to treat history-dependent materials, thanks to their suitability to modern hardware accelerators requirements [25, 20]. Indeed, parallel computing is a key capability for effective advancement of industrial-grade, large-scale computations, particularly in the fields of high-speed compressible computational fluid dynamics and Fluid-Structure Interaction (FSI, [32]) simulations. On the other hand, rapid hardware and software evolution makes researchers lean towards generic and portable implementations, which enables developers to adapt fast to sudden technology innovations.

In view of exponentially increasing High Performance Computing (HPC) resources and the method's accurate handling of a wide range of phenomena, MPM is becoming increasingly relevant for high-speed CFD and FSI simulations. In MPM, continuum media are discretized by means of Lagrangian particles, the *material points*, each one storing every state variable evaluated at its position, enabling the description of a wide range of materials [23, 43, 29] as well as large deformations [1, 52, 16] and fracture phenomena [53]. Notwithstanding its Lagrangian character, MPM also employs a background Cartesian grid to compute differential quantities and solve the motion equation, thus mediating the particle-particle interactions, and taking advantage of both Eulerian and Lagrangian approaches. These features make it an interesting candidate for the development of a highly parallel, Graphics Processing Units (GPUs)-based FSI solver. Indeed, in order to reach a high degree of efficiency, GPU-based solvers require a large degree of data locality and fine-level parallelism. MPM implementations can naturally achieve these, since:

- every GPU thread can manage up to very few grid cells or particles;
- the link between cells and particles can be easily built thanks to the structured character of the grid;
- accuracy in the discretisation of continuum bodies is obtained by means of the Lagrangian particles, so that the grid does not have to match the solid boundary.

Thus, there is no need of computationally expensive, unstructured,

moving or deforming meshes and a structured cartesian grid can be used instead, simplifying also techniques such as Adaptive Mesh Refinement and Domain Decomposition in a parallel context [47, 54]. Since MPM first introduction, various enhancements of the method were proposed, solving some of its drawbacks such as grid-crossing error [49] and volumetric locking [15], and improving its accuracy and conservation properties. To address instabilities which arise when particles cross the grid, variants of the method were proposed, such as GIMP [4], CPDI [39], iMPM [46] and IGA-MPM [34], and numerical analysis studies on the use of B-Splines as basis functions in MPM were conducted [42]. An affine and a polynomial mapping was later added to the B-Splines MPM [30, 21] resulting in an angular momentum-conserving model. Other studies explored least squares techniques [55] enabling the recovery of the affine/polynomial splines MPM [28], the effect of spatial and temporal discretization errors, and the application of symplectic integrators [5]. In light of these developments, MPM represents an effective method for the simulation of a wide range of materials and phenomena.

However, in spite of recent implementations for computer graphics applications [22, 54], MPM implementations on GPUs have not yet been applied to compressible fluid dynamics. In fact, even when addressing gas dynamics and solids mechanics, MPM has been used only for the solids, while the compressible fluid dynamic problem has been solved through a second order WENO scheme [11]; moreover, such implementation is run on CPUs. Existing studies on MPM for compressible flows focused on numerical convergence and error analysis [51] and on modelling and expanding the range of applications for the method [58, 44]. Nonetheless, to the best of the authors' knowledge, no studies exist that are dedicated to the GPU based, High Performance Computing aspects of MPM implementations for strongly compressible fluid dynamics problems.

In previous work [2] we ported an existing MPM algorithm [58, 57, 12] to CUDA-C [35], adapting it to GPUs architecture and obtaining promising speed-ups with respect to a C++ CPU version. The CUDA-C programming model was chosen because of its known performance capabilities on NVIDIA A100 GPUs [36, 8]. However, the model had shortcomings in its low-level character and specificity to the underlying architecture. In addition, while it can be made to work on, e.g., AMD GPUs via HIP with minimal changes, it cannot be ported to different architectures such as CPUs without substantial code modifications.

One of NVIDIA's solutions for performance portability involves its own C++ compiler `nvc++` [19, 37], using which one rewrites al-

algorithm steps relying on C++ Standard Template Library (STL), specifying a parallel execution policy. To give an example, in this framework it is possible to parallelize the following for loop:

```
1   for (index_t i = 0; i < n; ++i)
2       {do some operations}
```

into a call to a `for_each` with a proper lambda or functor, e.g.:

```
1   std::for_each (std::execution::par,
                  first_counting_iterator, last_counting_iterator,
                  [](index_t i){do some operations});
```

Although the approach does not prevent the developer from introducing data-races or deadlocks, the code can be written only once, and then, depending on the option specified during compilation, run in parallel on multicore CPUs or GPUs.

However, `nvc++` high-level features come at a price, as the developer loses the control on memory handling and, in particular, on when Host-to-Device and Device-to-Host memory copies are performed. The code runs on host, any invocation to an algorithm with a parallel execution policy expresses the developer's preference to run that algorithm in parallel. If compiled for GPUs, memory is copied to the device, computations are performed and then data is copied back to host. In physics and in engineering dynamics simulations, where each time step depends on the previous one, this means that the maximum reachable level of parallelization corresponds to a single call to a parallel algorithm inside a traditional for loop for time advancing. Since memory fetches can be significantly more costly than computations, this is suboptimal.

The present contribution expands the scope of [2] and overcomes the performance issues with `nvc++` by designing a portable MPM code for transonic and supersonic compressible gas dynamics based on Thrust [38], a C++ template library for CUDA based on the Standard Template Library (STL). In addition to `nvc++` features, Thrust introduces two types of STL like vectors, one for the host (typically, the CPU) and one for the device (typically, the GPU); this allows the user to specify when memory should be copied via explicit calls. For example, it's possible to perform a single Host to Device copy when reading the initial data file, and one Device To Host copy whenever saving partial results on output data files, strongly reducing execution time related to memory fetches.

Moreover, as additional portability-enhancing features included in the implementation:

- Thrust syntax is mostly compatible with STL syntax, adding just a few `define` preprocessor macros or templates. Thanks

to this, almost the same source code can be compiled for parallel execution on GPUs with NVIDIA CUDA compiler `nvcc`, on AMD GPUs with the AMD compiler for ROCmThrust, and on CPUs with `g++` and `clang++` compilers (when it is linked with a parallel library such as TBB, Intel’s Threading Building Blocks).

- Thrust itself allows for modifications to the default device and host system, so that it can be run serially and in parallel, with TBB or OpenMP on CPUs for the host, and also on the GPU via CUDA-C++ for the device only. The code can be compiled and executed on a CPU-only machine as well, provided CUDA is installed and `THRUST_DEVICE_SYSTEM` is defined to be `THRUST_DEVICE_SYSTEM_EM_{CPP,OMP,TBB}` at compilation stage.

Notwithstanding the portability objectives, we designed the code for optimization on modern graphics hardware accelerators and made further modifications to the original algorithm [12, 58]. For example, we:

- added treatment of obstacles in gas dynamics simulations,
- added a particle re-ordering step,
- postponed particles movement to the end of the time loop,

and thus values of basis function evaluated at previous particle positions don’t need to be stored and can be computed on the fly instead, which is cheaper on modern hardware accelerators.

Specific development choices are described that enable optimization on modern GPU-based HPC architectures and adaptability to different hardware, as well as generality of the approach for the purposes of its portability also towards different software. The accuracy and performance of the implementation are evaluated on a number of compressible flow benchmarks and results are compared with available approaches in the literature.

The paper is structured as follows. Section 2 contains the analytical and numerical formulation of the method. Section 3 describes the chosen algorithm and the current and implementation choices. Section 4 illustrates the results obtained on benchmark test cases, and the final section 5 contains a discussion of the results, draws the conclusions of the performed work, and prospects future developments.

2 Model Formulation

2.1 Model Equations and Weak Formulation

As mentioned, MPM takes advantages of both the Eulerian and the Lagrangian perspective; specifically, the Lagrangian particles discretisation approach affords flexibility in modelling various kind of phenomena and materials, while the Eulerian grid discretisation is beneficial for scalability as the grid allows the mediation of particle-particle interactions. For the mathematical modelling we choose the Lagrangian framework, and we model high speed gases as inviscid fluids in a domain Ω governed by the compressible Euler equations [24, 57]:

$$\begin{cases} \frac{d\rho}{dt} + \rho \nabla \cdot \mathbf{v} = 0 \\ \rho \frac{d\mathbf{v}}{dt} = \nabla \cdot \boldsymbol{\sigma} + \rho \mathbf{b} \\ \rho \frac{de}{dt} = \boldsymbol{\sigma} : \dot{\boldsymbol{\epsilon}} \end{cases} \quad (1)$$

where ρ , \mathbf{v} , $\boldsymbol{\sigma}$, $\rho \mathbf{b}$, p , e and $\dot{\boldsymbol{\epsilon}}$ represent respectively the mass density, the velocity, the stress tensor, the external forces density, the pressure, the specific internal energy and the strain rate tensor of the fluid.

In this work, we:

- enforce mass conservation by keeping constant the number of Lagrangian material points (particles) along the simulations, as well as each particle mass,
- choose to model the fluid as a bi-atomic perfect gas, governed by the state equation

$$p = (\gamma - 1)\rho e \quad (2)$$

where e is the specific internal energy and γ is the ratio between specific heat at constant pressure and constant volume, $\gamma = c_p/c_v = 1.4$ for a bi-atomic gas.

To derive the final discretisation of the equations, a weak form of the force balance expressed by the motion equation is derived [45, 44]:

$$\int_{\Omega} \rho \dot{\mathbf{v}} \cdot \mathbf{w} d\Omega = - \int_{\Omega} \boldsymbol{\sigma} : \nabla \mathbf{w} d\Omega + \int_{\partial\Omega} \boldsymbol{\tau} \cdot \mathbf{w} d\Gamma + \int_{\Omega} \rho \mathbf{b} \cdot \mathbf{w} d\Omega \quad (3)$$

where, $\dot{\mathbf{v}}$ denotes the total, or Lagrangian, velocity derivative, \mathbf{w} is a generic test function and $\boldsymbol{\tau}$ the stress on the surface. It is worth noting that it is possible to derive the same formulation also by

adopting the standard Finite Element procedure, provided material points are considered as moving quadrature points [17]. In fact, standard MPM can be seen as a modification of traditional FEM, in which the integration points are not related to the Finite Element mesh and are Lagrangian, and thus suitable for history dependent models too [12].

This dynamically comprehensive yet relatively simple equation set is chosen as it enables testing the performance portability of the MPM implementation on compressible gas dynamics benchmarks [50, 41] and comparison with existing approaches [58, 44].

In the following, we simplify further the model assuming the fluid to be inviscid, and thus the stress tensor to be due to pressure only, and we neglect external forces. Euler equations become:

$$\begin{cases} \frac{d\rho}{dt} + \rho \nabla \cdot \mathbf{v} = 0 \\ \rho \frac{d\mathbf{v}}{dt} = -\nabla p \\ \rho \frac{de}{dt} = -p \nabla \cdot \mathbf{v} \end{cases} \quad (4)$$

The continuity and energy conservation equations will be directly discretized and used to update particle properties in the algorithm (see section 3 and algorithm 1), while the discretisation of the weak form of the motion equation is treated in more depth in the next section.

2.2 Numerical Method

The link between the Eulerian grid and the Lagrangian particles is given by the Particle-to-Grid (P2G) and Grid-to-Particle (G2P) mappings, which are the building blocks of the computational algorithm, and that can be derived from the discretization of the weak form (3). The latter can be obtained expressing the mass density via of Dirac delta functions [44]:

$$\rho(\mathbf{x}, t) = \sum_{k=1}^{N_p} M_p \delta(\mathbf{x} - \mathbf{x}_p) \quad (5)$$

Here and in the following, when it is useful to distinguish, grid quantities are written in lower case Roman letters, while particle ones are written in either upper case Roman or Greek letters.

Particle-to-Grid and Grid-to-Particle mappings read [45]:

$$a = \text{P2G}(A; X, Y) := \left[\sum_{k=0}^{N_p-1} A_k u_i(X_k, Y_k) \right] \quad (6)$$

$$A = \text{G2P}(a; X, Y) := \left[\sum_{i=0}^{(nx+1)(ny+1)-1} a_i u_i(X_k, Y_k) \right] \quad (7)$$

$$\nabla a = \text{P2GD}(A; X, Y) := \left[\sum_{k=0}^{N_p-1} A_k \nabla u_i(X_k, Y_k) \right] \quad (8)$$

$$\nabla A = \text{G2PD}(a; X, Y) := \left[\sum_{i=0}^{(nx+1)(ny+1)-1} a_i \nabla u_i(X_k, Y_K) \right] \quad (9)$$

where $u_i(X_k, Y_k)$ denotes the basis function of the solution space and test functions space centred on the i -th grid node and evaluated in the k -th particle position, a is a generic grid variable, A is its particle counterpart, N_p is the number of particles, nx, ny are the cell numbers in the x and y direction and D stands for derivative. For the numerical discretisation of the Eulerian aspects of the method, we choose a Cartesian grid of quadrilateral elements. Among the possible choices, this one lends itself naturally to computationally efficient refinements through a quad-tree approach [40]. Moreover, we opt for Lagrangian hat functions as basis for the functional spaces of both the solution and the test function, setting our treatment in a \mathbb{Q}_1 framework.

This approach corresponds to bilinear weighting function of standard MPM, and is known to cause volumetric locking and spurious oscillations in the computed quantities. The reason can be easily understood by the above equations: when u is (bi)-linear, ∇u is constant, but potentially different in neighbouring cells. Thus, when crossing cells, particles might experience discontinuous solicitations. This issue can be numerically tackled with many strategies, among which adding artificial viscosity [56] or choosing higher order basis functions. For simplicity of implementation, we choose the first, leaving the second for a future work.

With respect to standard MPM [57, 12], the present algorithm adds a step to take into account the flow around obstacles. Namely, we subtract the inward component of both linear momentum and force from the grid nodes whose cell is marked as an obstacle cell in following equations (stemming from the method for granular materials [3]):

$$(m\mathbf{v}_i^o)' = m\mathbf{v}_i^o - \frac{m\mathbf{v}_i^o \cdot \mathbf{n}_i^o - |m\mathbf{v}_i^o \cdot \mathbf{n}_i^o|}{2} \mathbf{n}_i^o \quad (10)$$

$$(\mathbf{f}_i^o)' = \mathbf{f}_i^o - \frac{\mathbf{f}_i^o \cdot \mathbf{n}_i^o - |\mathbf{f}_i^o \cdot \mathbf{n}_i^o|}{2} \mathbf{n}_i^o \quad (11)$$

where the subscript denotes the i -th grid node, the superscript o stands for obstacle and \mathbf{n} is the normal unit vector, positive if

directed outward from the obstacle.

Normal unit vectors to a domain profile $\partial\Omega$ are computed as gradients of the Signed Distance Function, defined as:

$$sd(\mathbf{x}) = \begin{cases} -\inf_{y \in \partial\Omega} d(\mathbf{x}, \mathbf{y}) & \mathbf{x} \in \Omega \\ \inf_{y \in \partial\Omega} d(\mathbf{x}, \mathbf{y}) & \mathbf{x} \notin \Omega \end{cases} \quad (12)$$

where $d(x, y)$ is the Euclidean distance. Taking the gradient yields:

$$\nabla sd(\mathbf{x}) = \mathbf{n}(\mathbf{x}) \quad \mathbf{x} \in \partial\Omega \quad (13)$$

An algorithm for signed distance function computation can be found in [9].

Finally, we use explicit time integration [12], whose stability is subject to a CFL criterion:

$$\Delta t < \alpha \frac{\Delta x_{min}}{v_{max}} \quad (14)$$

where α collects constants. The range of admissible time steps is bounded from above by the ratio between the smallest grid cell dimension Δx_{min} and the highest speed v_{max} , considering both particles velocity and speed of sound $c_s = \sqrt{\gamma \frac{p}{\rho}}$. The efficiency cost of enforcing small time steps is balanced by the need of resolving fast dynamics. In addition, explicit-in-time methods sidestep the need to solve global linear systems at each time step, thus enjoying better scalability properties than implicit methods.

3 Portable MPM Implementation

This section describes the algorithm that was presented in section 2 and how it was implemented to ensure portability on different architectures and efficiency on GPUs. The development of the code benefited in part from publicly available Open Source libraries: Thrust¹, JSON², and quadgrid³. In detail, the algorithm implementation is composed of the following steps:

1. Data generation: the creation of simulations input is performed separately from code execution. For simple geometries it is handled via ad-hoc C++ scripts. For complex geometries requiring a careful computation of the signed distance function, an Octave script is used instead, to take advantage of

¹<https://github.com/NVIDIA/cccl/tree/main/thrust>

²<https://github.com/nlohmann/json>

³<https://github.com/carlosedfalco/quadgrid>

Octave built-in functions. In both cases, since objects are considered at rest, normal unit vectors are computed only once, and boundary cells are marked with a flag corresponding to the boundary condition. Finally, the initial data file is saved in JSON format.

2. MPM class object construction: since the most computationally costly operations are the memory related ones, such as I/O and copies between host and device, a class object for the method is constructed only once, reading grid and particles data from the input file, data is saved on host memory and copied to device memory. So doing, is possible to construct functor objects which will be called on the device during the time loop, without the need of further copies.
3. The time advancing loop starts; inner steps, except from output operation, are implemented as Thrust or STL `for_each`s, depending on the architecture chosen at compile time.
 - (i) Grid variables are reset and current grid variables are overwritten with the ones saved during construction stage, performing a device to device copy. This step can be performed since all history dependence is maintained by Lagrangian particles.
 - (ii) Equations (6) and (8) are applied to map particles mass, momentum and force to the grid.
 - (iii) Boundary conditions are enforced on grid nodes momentum and force. Specifically, at each time step and for each boundary node marked as of obstacle type, inward components of momentum and force are subtracted as in equations (10) and (11).
 - (iv) Grid nodes momentum is advanced in time.
 - (v) Velocity and acceleration G2P (7) is applied, and next, velocity is updated. Acceleration itself is not stored, but computed as the result coming from a local G2P of the relevant nodes ratio between force and mass. Following standard MPM [12], we store the G2P velocity in a temporary velocity vector $\bar{\mathbf{V}}$ and don't use it to update particles velocity; however, we postpone its usage.
 - (vi) Momentum P2G (6) is performed.
 - (vii) Boundary conditions on the updated grid values are enforced.
 - (viii) Particles strain rate tensor (velocity gradient) is computed as the G2PD (9) of the ratio between grid nodes momentum and mass, and then particles properties are updated.

- (ix) Particles position are updated using $\overline{\mathbf{V}}$. Thus, the time advancing scheme is the same of [12]. However, particles moving is postponed, so that, in all the above steps, basis functions and their gradient can be computed on the fly, without the need to store the value they had at former particles position.
- (x) Particles-to-grid connectivity map is updated with new positions - this step is computationally efficient also thanks to the choice of a Cartesian grid.
- (xi) Only if the initial data options ask for N intermediate outputs, a device to host memory copy and an output from host to disk are performed at N moments equidistant in time.
- (xii) Optionally, a re-ordering algorithm is applied to keep data locality, i.e. to keep contiguous particles in the physical simulation also close in memory. The algorithm is based on an indexing vector built iterating over the structure that stores information about which particles are contained in every grid cell, such that the n -th element of the ordering vector indicates the current sorting particle index which has to be at n -th position after re-ordering.
- (xiii) A control on the CFL condition (14) is enforced, taking into account particles velocity (momentum over mass and $\overline{\mathbf{V}}$) and the speed of sound.
- (xiv) Time step is updated, loop ends.

4. A final device-to-host memory copy and output is made.

Algorithm 1 summarise the for loop procedure.

Algorithm 1 Time loop sketch

1: **while** $t < t_f$ **do**

2: Grid reset

3: Mass, momentum and force P2G

$$m = \text{P2G}(M), \quad m\mathbf{v} = \text{P2G}(M\mathbf{V}), \quad \mathbf{f} = \text{P2GD}(P\frac{M}{\rho})$$

4: Boundary conditions enforcement on $m\mathbf{v}$, \mathbf{f} & obstacle treatment as in (10), (11)

5: Momentum equation solution on the grid

$$(m\mathbf{v})' = m\mathbf{v} + \Delta t \mathbf{f}$$

6: G2P mapping

$$\bar{\mathbf{V}} = \text{G2P}(\frac{m\mathbf{v}}{m}), \quad \mathbf{A} = \text{G2P}(\frac{\mathbf{f}}{m})$$

7: Velocity update

$$\mathbf{V}' = \mathbf{V} + \Delta t * \mathbf{A}$$

8: Momentum P2G

$$m\mathbf{v} = \text{P2G}(M\mathbf{V})$$

9: Boundary condition enforcement on $m\mathbf{v}$

10: Particles properties update:

$$\nabla \mathbf{V} = \text{G2PD}(\frac{m\mathbf{v}}{m})$$

$$E' = E + \Delta t \frac{-P}{\rho} \nabla \cdot \mathbf{V}$$

$$\rho' = \frac{\rho}{1 + \Delta t \nabla \cdot \mathbf{V}}$$

$$P' = (\gamma - 1)\rho' E'$$

11: Particles moving $\mathbf{X}' = \mathbf{X} + \Delta t \bar{\mathbf{V}}$

12: Optional particles re-ordering

13: CFL condition (14) check & time advance

14: **end while**

This algorithm is of special interest for acceleration on GPUs since it can be written in terms of the four kernels (6), (7), (8), (9), which presents interesting parallelisation potentialities. Grid-to-Particles operations are intrinsically Single Instruction Multiple

Data (SIMD) parallelizable, since data is projected from grid nodes to particles, and thus particles are independent from one another during writing stage. Particles-to-Grid kernel presents the same potentialities, however, if they are implemented strictly following their analytical definition, they present a data race: different particles need access in both read and write mode to the same grid nodes.

In this work, we chose to patch the P2G and G2P kernels written in the external quadgrid library to adapt them to GPU execution via Thrust rather than writing ad hoc versions in the code, at the expense of some further optimisation that could have been added by exploiting the peculiarities of our test cases, to arrive at more general and portable conclusions. In any case, preliminary tests have shown that applying a kernel-fusion approach [38] where possible would not have affected the execution time order of magnitude.

A P2G implementation is then based on the following pillars:

1. The definition of a functor for each kernel. For example, the initial P2G on mass could be implemented as follows:⁴

```

1 struct functor_t
2 {
3     real_t hx, hy;
4     real_iter_t x, y, M, m;
5     idx_iter_t ptcl_to_grid;
6     functor_t (){};
7     void operator () (idx_t k)
8     {
9         real_t N = 0.0, xx = x[k], yy = y[k];
10        idx_t row = grid_to_row (ptcl_to_grid[k]);
11        idx_t col = grid_to_col (ptcl_to_grid[k]);
12        for (idx_t inode = 0; inode < 4; ++inode)
13        {
14            N = shape_function (xx, yy, inode, col, row, hx,
15                               hy);
16            idx_t i = global_node(inode, col, row);
17            m[i] += N * M[k];
18        }
19    }

```

⁴To compile CUDA or Thrust device code decorators are necessary; for example, the functor could be modified as: `__device__ void operator () (idx_t k)`, and the `__device__` macro could be defined as empty during compilation for portability, in case a non-CUDA aware compiler is used for different architectures.

```
19 };
```

2. The definition of the proper counting iterators (or ranges), for example, following Thrust or Boost Libraries:

```
1 counting_iterator <idx_t> first_p(0), last_p(
    num_particles);
```

3. The call to the generic algorithm, e.g.:

```
1 for_each (execution_policy, first_p, last_p,
    functor);
```

Step 3 is the one that requires care when performed with a parallel execution policy. Indeed, it requires the handling of possible data races. Currently, we handle them through atomic operations, namely, in the above snippet we substitute `m[i] += N * M[k]` with `atomicAdd (&m(i), N*M[k])`, having re-defined `m` as a `real_t*`, and:

- relying on CUDA implementation of `atomicAdd` for execution on the GPU,
- and defining an ad-hoc `atomicAdd`, based on STL `std::atomic_ref`, for parallel execution on the CPU.

Atomics cost is not detrimental for overall performance on the GPU, and portability to non-CUDA backends is easily obtained, taking care of defining the ad-hoc `atomicAdd` for the CPU in such a way to be compliant with CUDA's API. However, in Section 5 we propose an alternative algorithm which avoids the data-race and thus the need of atomics in P2G like kernels.

4 Benchmarks

In this section we show the results of 2D numerical simulations of gas dynamics obtained with the described implementation of MPM, with a focus on supersonic gas flow over solid obstacles. A first general evaluation of accuracy is followed by an assessment of the sensitivity of the results to the choice of numerical parameters. We then test the efficiency and performance of the implementation in providing parallel scalability on GPU and its portability to CPUs. The experiments were carried out on NVIDIA A100-40 GPUs and AMD EPYC Rome 7402 CPUs at Leonardo S.p.A.'s in-house HPC facility *davinci-1*.

4.1 Test cases

We adopt non-dimensional units as in [41], and we model the fluid as a perfect, bi-atomic gas, with specific heat ratio:

$$\gamma = \frac{c_p}{c_v} = 1.4 \quad (15)$$

In the far field away from the obstacles, we set fluid density and pressure as:

- $\rho_\infty = 1.4$;
- $p_\infty = 1$;

where the subscript ∞ denotes unperturbed conditions. Thus, we obtain a unitary speed of sound:

$$c_{s,\infty} = \sqrt{\gamma \frac{p_\infty}{\rho_\infty}} = 1 \quad (16)$$

and an unperturbed Mach number equal to the reference speed:

$$M_\infty = \frac{v_\infty}{c_{s,\infty}} = v_\infty \quad (17)$$

For time integration, we enforce the time step to be:

$$\Delta t \leq \frac{1}{2} \frac{h_{min}}{v_{max} + c_{s,max}} \quad (18)$$

This requirement is more conservative than necessary, and, in the limits of the CFL condition, could be partially relaxed. However, we choose it to guarantee that particles can't move across more than one grid cell per time iteration; so doing, in the framework of our algorithm, we avoid the risk that particles pass through any boundary, and ensure that their motion will respect boundary conditions. In all test cases, initial particles position is sampled by a uniform random distribution in the fluid domain; in the following, we denote with ppc the average number of fluid particles per fluid cell, with N_C the total number of cells, and with N_P the total number of particles.

Supersonic flow past solid obstacles First, we consider two cases of supersonic, Mach 3 flow:

- (a) past a cylinder of radius 0.25 and centre (0.6, 1) in a $[0, 4] \times [0, 2]$ rectangular domain; and
- (b) past a rectangular-shaped step $[0.6, 3] \times [0, 0.2]$ in a $[0, 3] \times [0, 1]$ rectangular domain.

In both cases, we enforce wind tunnel-like boundary conditions, with inflow conditions at the left vertical boundary, outflow conditions at the right horizontal boundary, and slip conditions at the top and bottom boundaries.

Specifically, we set:

- $\mathbf{v}_{inflow} = (3, 0)$
- $\mathbf{v}_{top} \cdot \mathbf{n} = \mathbf{v}_{bottom} \cdot \mathbf{n} = 0$

where \mathbf{n} denotes the unit normal vector. A particles-recycling approach is adopted, whereby particles leaving the domain at the outflow boundary are regenerated in a random cell at the inflow boundary with inflow conditions, keeping the total particles number constant throughout the simulation.

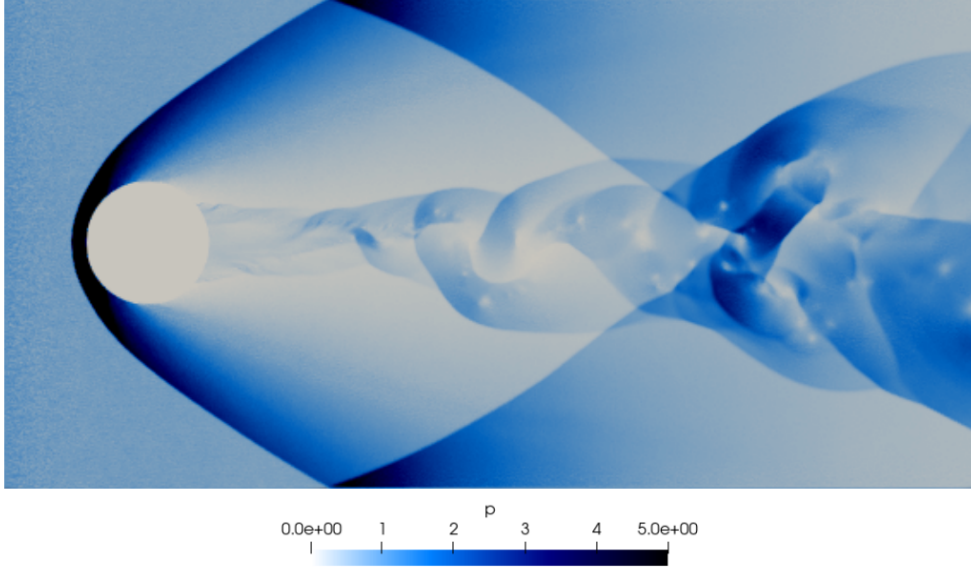


Figure 1: Mach 3 flow past a cylinder: pressure at $t = 10\,s$, $N_C = 10^6$, $ppc = 16$, $N_P = 15.6 \cdot 10^6$, artificial viscosity as in [56].

In test case (a), as gas particles travel past the cylinder, a shock wave develops at the front and two oblique shocks in the rear. The first shock is reflected by walls and interacts with the back shocks; see Figure 1 and its caption for numerical details.

In the step test (b), a frontal shock develops that is later reflected from the top wall and successively from the step see Figure 2 and its caption for numerical details.

The MPM implementation is able to correctly simulate the main flow features, in case of both round shapes and sharp edges and corners. Computed shock-waves angle and flow deflection angle (Figure

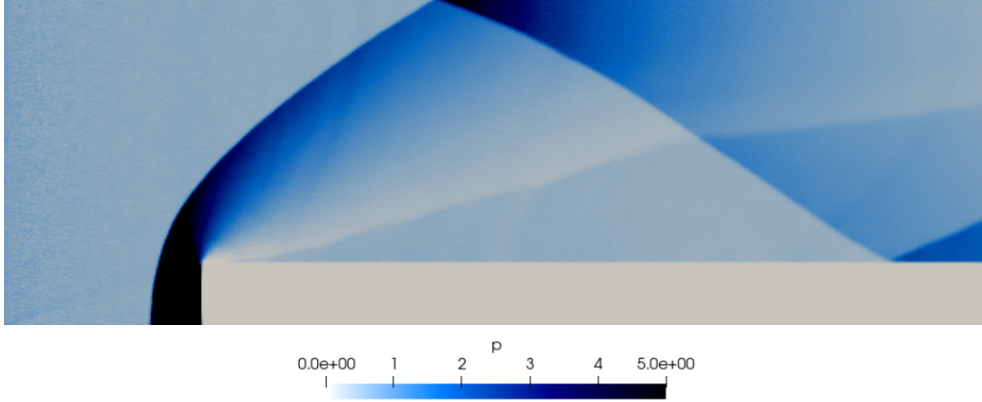


Figure 2: Mach 3 flow past a step: pressure at $t = 12s$, $N_C = 326.7 \cdot 10^3$, $ppc = 16$, $N_P = 4.4 \cdot 10^6$, artificial viscosity as in [56].

1) are found to be in agreement with experimental references [18] as well as with results with other codes, e.g., deal.II, when the same polynomial order is used for basis functions⁵. The lower level of detail in comparison with some results in the literature ([14, 33, 24]) is likely due to the first order space discretisation used here.

Transonic flow past an aerofoil Next, we test the method in simulating flow past an OAT15a aerofoil at Mach 0.73, to assess the ability of the implementation in dealing with more complex-shaped obstacles. The signed-distance function approach, in conjunction with the implemented obstacles treatment (10),(11), naturally fits the aerofoil profile (Figure 3). Since, rather than using an analytic expression, the profile and its normal unit vectors are generated reading from a file containing a set of points, the method proves to be sufficiently general and not bounded to particular geometric shapes.

⁵https://www.dealii.org/current/doxygen/deal.II/step_69.html#Results

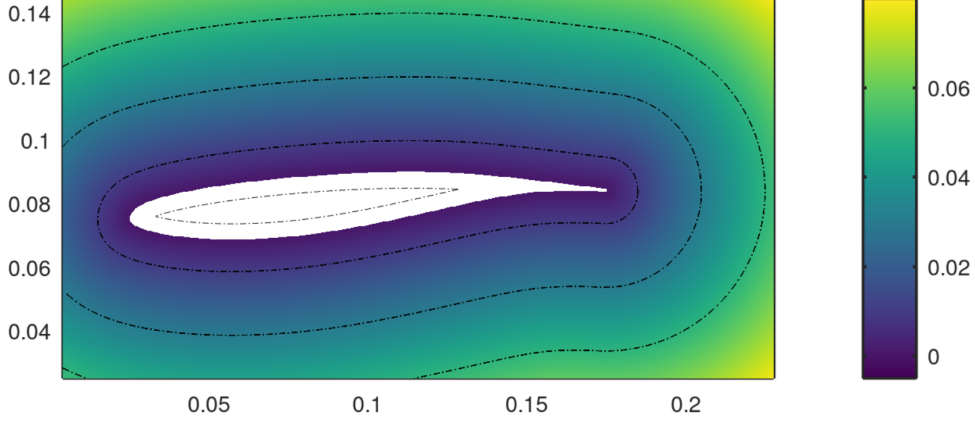


Figure 3: Signed distance function for OAT15a aerofoil at $\alpha = -3.5^\circ$

Within the $[0, 0.4] \times [0, 0.27]$ domain, we enforce inflow conditions at the left boundary, with

$$\mathbf{v}_\infty = (0.73, 0) \quad (19)$$

and outflow conditions at other boundaries. To test the physical reliability of the approach, we choose a large attach number to emphasise dynamical effects and display velocity magnitude and streamlines (Figure 4).

These are found to be in line with what is expected from physical considerations: we can see airflow speeding up as it approaches the aerofoil, with an higher velocity magnitude in the top area with respect to the bottom one.

Taylor-Green vortex In the third test, we address the Taylor-Green Vortex test case, a well studied, fluid-only benchmark to assess both viscous and inviscid fluid dynamics codes in the literature, usually at subsonic regime ([10, 6, 48]); here we simulate the case in supersonic Mach 3 conditions.

In the inviscid case, the dynamics is strongly affected by problem symmetries, leading to “impermeable box boundary conditions” [6]. These symmetries are:

- within the $[0, \pi]^2$ square-shaped computational domain, the fluid never crosses the lines $x = n\pi$ and $y = n\pi$; and
- close to the boundaries, both the normal velocity \mathbf{v}_\perp and the normal derivative $\frac{\partial \mathbf{v}_{//}}{\partial \mathbf{n}}$ of the tangential velocity $\mathbf{v}_{//}$ vanish.

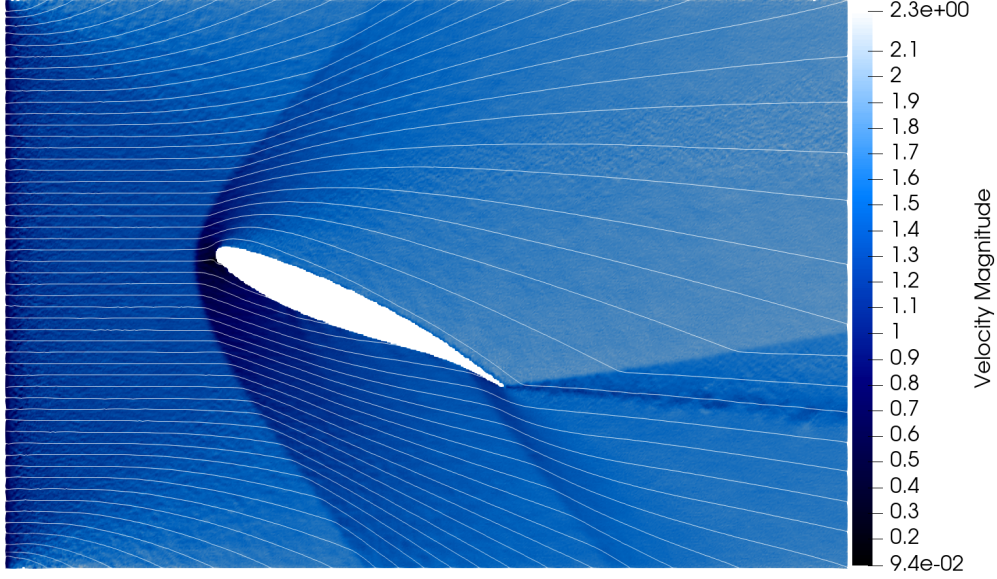


Figure 4: OAT15a Mach 0.73 flow: velocity streamlines at $\alpha = 25^\circ$, $t = 1s$, $N_C = 247 \cdot 10^3$, $ppc = 9$, $N_P = 2.18 \cdot 10^6$, artificial viscosity as in [56].

We then set the initial conditions:

- $v_x(x, y) = v_\infty \sin\left(\frac{x}{\pi}\right) \cos\left(\frac{y}{\pi}\right)$;
- $v_y(x, y) = -v_\infty \cos\left(\frac{x}{\pi}\right) \sin\left(\frac{y}{\pi}\right)$;
- $p(x, y) = p_\infty + \frac{\rho_\infty}{16} \left(\left(\cos\left(\frac{2x}{\pi}\right) + \cos\left(\frac{2y}{\pi}\right) \right) \cdot 3 - 2 \right)$.

The numerical method captures the flow features with good accuracy as compared to results in the literature (Figure 5, cf. Figure 1b in [6]), confirming the general applicability of the MPM algorithm in simulating compressible fluid flow.

4.2 Sensitivity to numerical parameters

Having addressed the applicability of the method to high speed, compressible gas dynamics, we focus on the cylinder test case and test the dependence of the results on key numerical parameters. Specifically, we vary the number of grid cells, N_C , and the average number of particles per cell, ppc , and evaluate the effect on numerical stability and shock-capturing ability.

First, sufficiently high spatial resolution must be used to resolve shocks, otherwise the scheme becomes too diffusive. For the cylinder test case, testing evidence suggests that this minimum resolu-

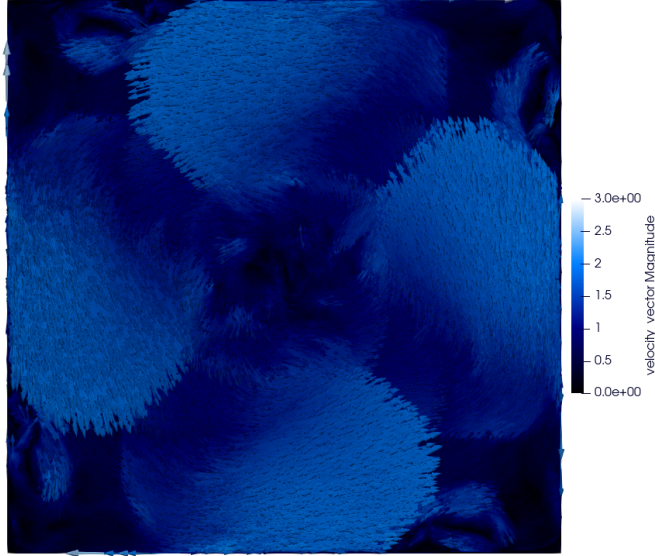


Figure 5: Taylor-Green vortex: computed velocity at $t = 2s$, $N_C = 3.94 \cdot 10^5$, $ppc = 9$, $N_P = 3.55 \cdot 10^6$, artificial viscosity as in [56].

tion amounts to around 3500 cells. Besides resolution, supersonic compressible fluid dynamics requires further care in setting the average number of particles per cell. Indeed, ppc affects stability in a twofold fashion. First, for low ppc values (e.g., 1), widespread oscillations are observed all along the simulation, due to almost randomly distributed empty cells. In a recent study, a ppc value of 4 was found to be optimal for convergence of gas dynamics tests at lower speed [44], and, indeed, a $ppc = 4$ solves this issue. However, for supersonic flow past a static obstacle, we observed that using $ppc = 4$ might cause the formation of domain regions of empty or quasi-empty cells, which gets evident as grid resolution increases, during the initial transient phase from uniform, undisturbed conditions, as can be seen from Figure 6. Such emptying causes later formation of nonphysical cavitation-like effects during the transient that precedes equilibrium, which alter the dynamics, and, if particularly strong, can cause also spurious shock waves, that interact with the physical ones. These events can be prevented by increasing the average particles per cell number: at Mach 3, spurious shock waves become less relevant with $ppc = 9$, and undetectable with $ppc = 16$.

These effects, and in particular strong disruptions, are of no interest here, since the initial transient phase is non-physical, and derives only from the choice to start the simulations with undisturbed inflow

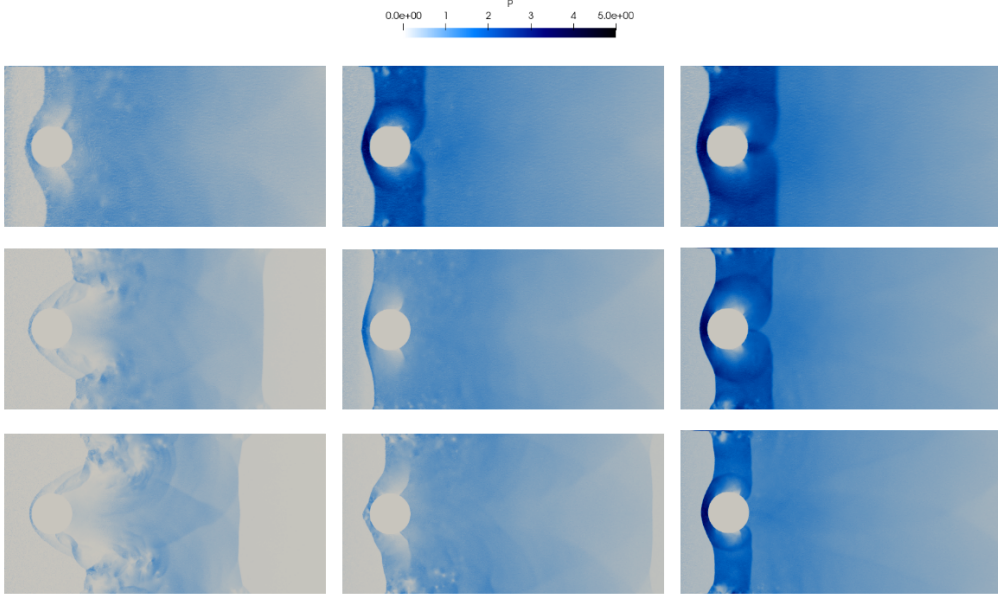


Figure 6: Mach 3 flow past a cylinder test case, various settings: from the first to the third row, N_C changes from 10^5 to $5 \cdot 10^5$ and 10^6 ; from the first to the third column, ppc changes from 4, to 9 and to 16.

conditions and particles position sampled from a uniform random distribution instead that from a previously computed equilibrium condition, e.g. the result of an already converged simulation. However, it could be a relevant aspect if fast changing dynamic situations have to be simulated, for example with a moving cylinder in a FSI framework, since they would alter its dynamics. In such cases, a sufficient number of particles per cell should be used. By contrast, a $ppc = 4$ value can be employed when simulating equilibrium conditions: numerical experiments show that equilibrium is reached notwithstanding spurious instabilities in the initial transient phase (see Figure 7 for a snapshot).

However, for linear grid basis functions, numerical oscillations are present for any ppc value. Therefore, additional artificial viscosity is essential to compute numerical quantities, even though going high order might be necessary to properly resolve fine structures. For example, in the cylinder test case the standard deviation on pressure, temporally averaged over enough different equilibrium instants, can decrease by about one half with the addition of a proper artificial viscosity (Figure 7 shows also effects of numerical viscosity on a single snapshot).

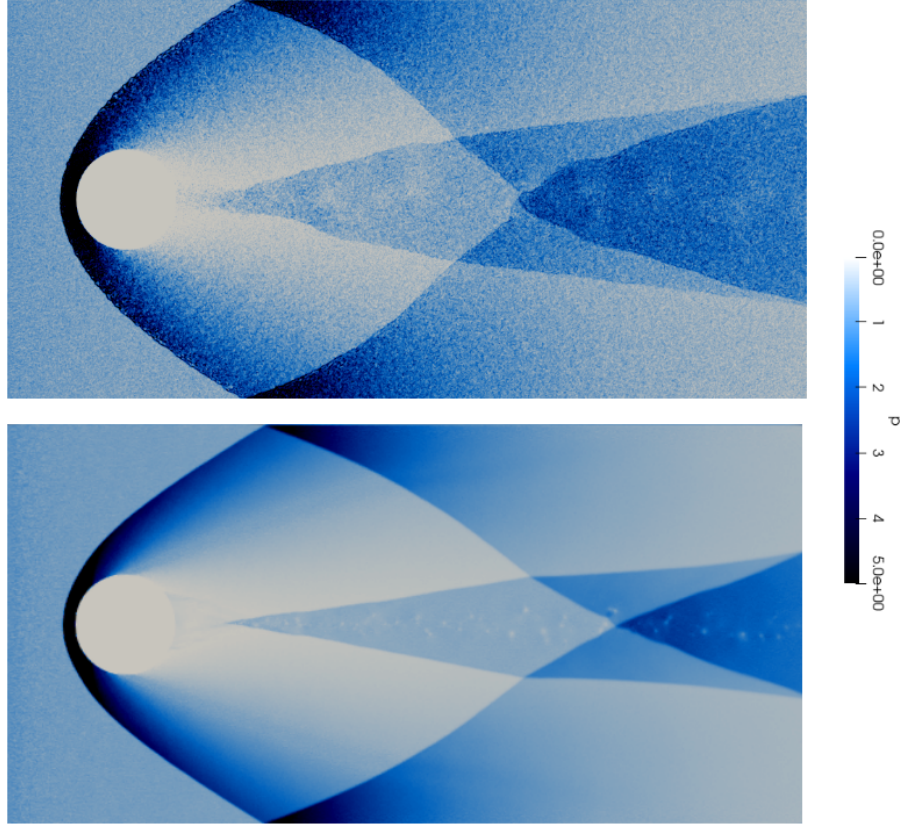


Figure 7: Mach 3 flow past a cylinder test case, equilibrium snapshot with $N_C = 10^5$, $ppc = 4$ and no artificial viscosity (above), and $N_C = 10^6$, $ppc = 16$ and artificial viscosity. Despite the very different setting, which determines a different initial behaviour, the two simulations foresee according pressure around the cylinder at equilibrium, and only slight differences in the far rear.

Finally, a sufficient randomness of particles position, especially in particles recycling, is fundamental to obtain stable and physically meaningful simulations, in agreement with results in the literature on Particle-In-Cell methods in plasma physics. On longer runs (i.e. above tens of physical seconds) a symplectic time integration scheme might be useful [31].

4.3 Computational performance

We then focus on the computational performance and scalability of the method, analysing the computational time required by simulations when varying the grid resolution and *ppc* values. It is worth noting that the implemented parallel kernels can be particle- or grid-based, and, respectively, assign one particle or one grid node to one GPU thread. Moreover, we implemented both mapping kernels (P2G and G2P) as particle-based kernels, since this proved to be the most efficient option.

First, a detailed profiling of each step of algorithm 1 reveals that the G2P and the P2G kernels take up 85% of the parallel part of the code and more than 60% of the whole computational time. This is due both to the relative complexity of those two kernels and to the high number of times they are called per algorithm iteration. We thus focus the scalability analysis on these kernels.

The first finding is that both kernels scale linearly with the total number of particles, in agreement with their implementation (Figures 8 and 9), while pure grid kernels, such as boundary conditions enforcement, scale with the number of nodes. For this reason, we applied a global particles reordering step in the algorithm and studied its effects on performance. Indeed, the ordering is done so that particles which are in the first grid cell after moving are assigned the lowest global indices, followed by those in the second grid cell, and so on moving along the grid. Thus, data which will be accessed at the next time iteration will be ordered, with contiguous particles having contiguous indexes, keeping data locality across the simulation, which is of utmost importance on our target architecture. The reordering turns out to have a significant impact on the G2P kernels, resulting in a further 4x speed-up factor, while preserving the linear scaling (Figure 8).

By contrast, the reordering appears not to have an appreciable effect on the P2G kernels, with slowdowns and accelerations evident at different particle values (Figure 9). The reason can be found in the main implementation difference among the two kernels. P2G introduces a data race, that is currently dealt with using CUDA’s atomi-

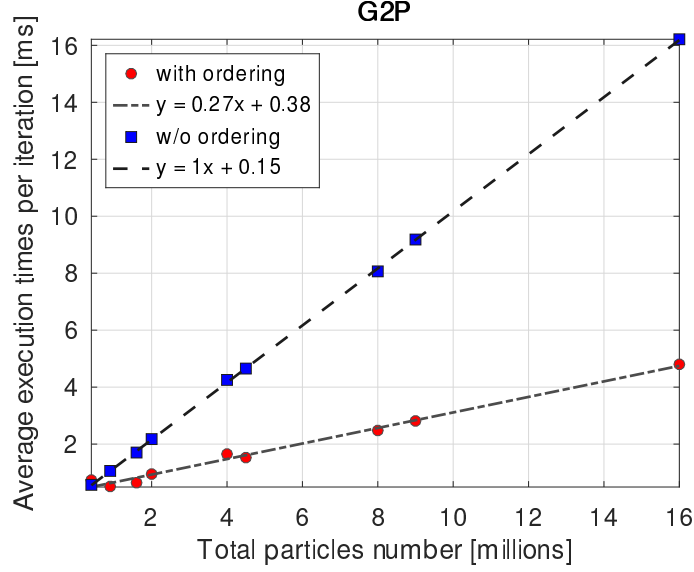


Figure 8: Profiling of main computational kernels: G2P kernels execution time is compared for the cylinder test case, varying N_C and ppc , considering also re-ordering effects.

cAdd, and its cost becomes more apparent with re-ordering. Indeed, even though, to the best of the authors' knowledge, NVIDIA's A100 scheduler policy is not accessible, numerical examples appear to suggest that the scheduler behaves more in a round-robin fashion rather than in a block partitioning way. So, a particle is assigned to a GPU thread, until there are some free, then a second particle is assigned, and so on. In this framework, randomisation of the global order of particles is somewhat beneficial, since it lowers the probability that particles that are in the same cells are processed simultaneously. After reordering, particles close in the domain are also close in memory, enhancing probability of a memory collision, i.e. of simultaneous access to the same data. Since in our case such access would be in read-and-write mode, it activates the atomic operation and degrades performance.

This also explains why reordering appears to not being beneficial for P2G kernels. Since a higher number of ordered particles per cell increases the chance of data races, the average number of particles per cell becomes an important parameter. Indeed, grouping simulations results per ppc value, we recover linearity, and can also confirm the trend of worsening performance at larger numbers of ordered particles in a cell. Indeed, comparing the linear fits in Figure 10, we can see that in the $ppc = 4$ and $ppc = 9$ cases execution is

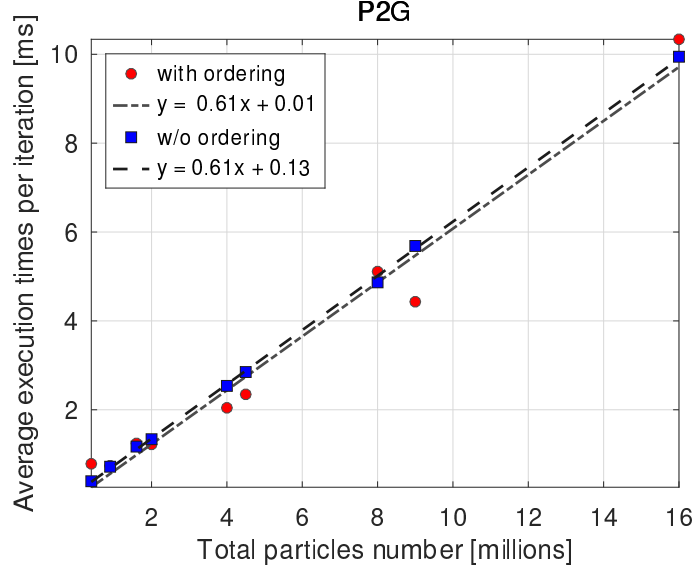


Figure 9: Profiling of main computational kernels: P2G kernels execution time is compared for the cylinder test case, varying N_C and ppc , considering also re-ordering effects.

faster than in the global fit, and in the $ppc = 16$ case it is slower.

Portability Finally, we test the application of the developed implementation also on a different architecture and compare the performance, addressing the performance portability of the MPM code. Specifically, we execute the cylinder test case on 2×24 CPU cores, running the nine numerical settings described above, without enforcing particles re-ordering, varying the number of cells and of particles per cell and studying how this affects the main computational kernels (Figure 11).

While portability is automatically granted, CPU performance turns out to be worse than single-GPU performance, even though 2×24 CPU cores are employed in parallel. This is consistent with expectations that MPM is better suited to GPU architectures.

As for the computational kernels:

- P2G kernels scale almost linearly with the number of total particles, in agreement with the beneficial effect of randomisation in reducing the actual execution of atomic operations;
- G2P kernels maintain quasi-linear scaling only if the average particles-per-cell number is kept fixed;
- the execution time required by all the other kernels considered

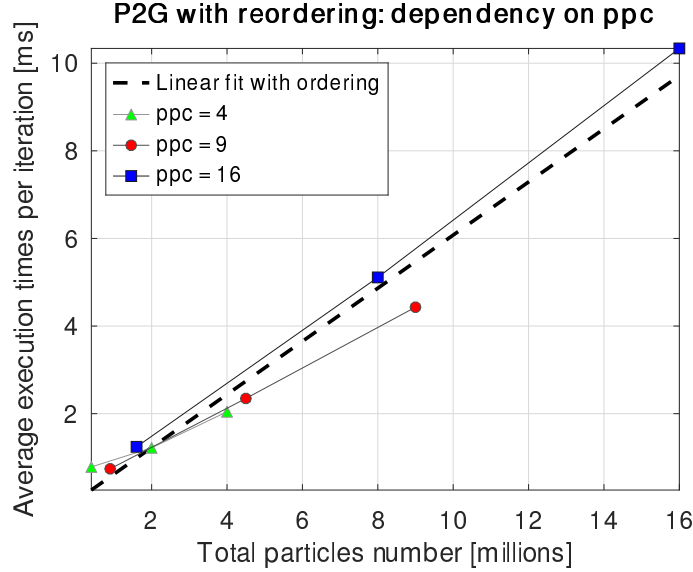


Figure 10: Profiling of P2G kernels: effect of average particles per cell number on version with re-ordering.

together is considerably smaller than the time required by P2G and G2P ones. This confirms the computational relevance of P2G and G2P also on different hardware.

The main difference with respect to the GPU test lies in the comparison between P2G and G2P performance, with the former significantly slower than the latter on the CPU. This is most probably due to our choice of writing an ad-hoc `atomicAdd` function, based on `std::atomic_ref`, with the same signature of the more performant CUDA's `atomicAdd`, to enhance portability and guarantee parallelism. An algorithm to directly avoid the data-race present in P2G-like kernels, and, thus, to provide a natively portable, parallel and atomic operation free implementation, is proposed in the next section.

5 Discussion and conclusion

This paper has showcased the potential of a performance portable implementation of the Material Point Method for compressible flows. Insight has been given on algorithm adaptations which will provide further benefits, moreover, the simulation of standard test cases of supersonic flow has provided results comparable with the literature and with established software runs with the same polynomial order

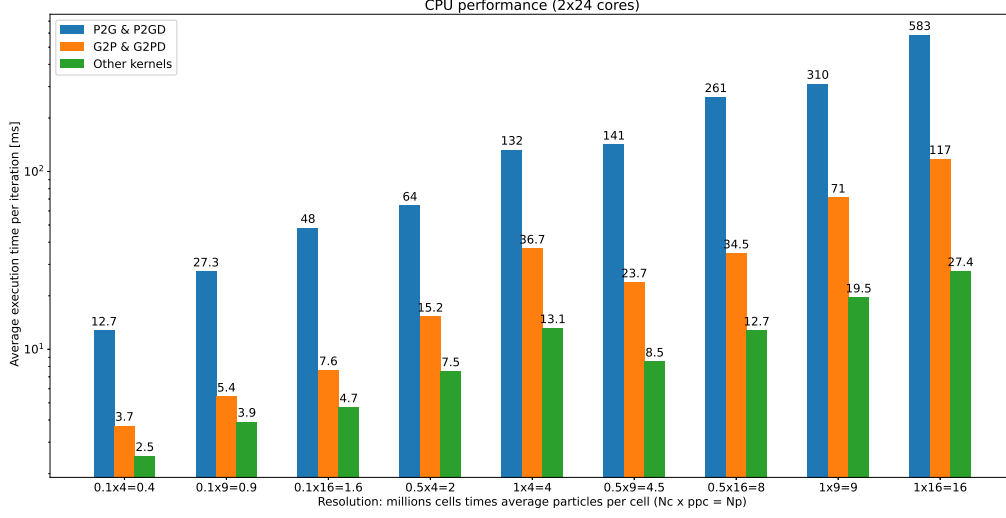


Figure 11: Profiling of main computational kernels: total G2P and P2G kernels execution time is compared for the cylinder test case, varying N_C and ppc , without re-ordering, on 2×24 CPU cores.

(first order - Lagrangian hat functions) and number of degrees of freedom. These results show that MPM is able to simulate Mach 3 gas dynamics, giving qualitatively good results with a prototype developed modifying existing implementations [58, 12], and serve as further step towards the design of a highly efficient MPM-based supersonic FSI solver.

As known from the literature [57, 42] and as also noted in a previous implementation [2], Q1 MPM suffers from strong numerical oscillation issues, especially in the vicinity of shocks. The issue is tackled in this paper by adding numerical viscosity in the form of additional terms in the momentum equation [56]. A more natural and accurate choice could be obtained by using quadratic B-Spline basis functions [49, 17], a code feature which is currently under development.

Performance tests on NVIDIA A100 GPUs have confirmed that the main computational steps of the MPM algorithm are the Particles-to-Grid and Grid-to-Particles kernels, and that they scale well with the size of the problem. Moreover, adding a reordering step is beneficial to data locality and, consequently, performance, while data races in the P2G kernel can be tackled CUDA’s atomics at acceptable cost, even though alternative exist. Last, this approach has shown to be easily portable to different hardware architectures, as CPUs.

Several future developments are planned in connection with the implementation and modelling choices made in this paper:

- On the modelling side, more complex test cases could be simulated, eventually leading to a 3D extension and Fluid-Structure Interaction models. In addition, the effect on parallel performance of higher order B-Splines under development will need to be carefully investigated.
- For the algorithm implementation, the use of CUDA atomic operation of GPUs choice was chosen for simplicity, also because it shown an acceptable impact on computational time and scalability (section 4). To reach the full parallelisation capabilities proved by the G2P kernels also for the P2G ones, P2G algorithm adaptations will be necessary. An attractive and more portable route would involve avoiding atomics, and writing a *grid colouring* algorithm that can be implemented in an architecture-independent way, relying only on standard libraries functions. Its main steps are:
 1. Build grid-to-particle connectivity
 - (i) Sort particle IDs by cell index
 - (ii) Count particles per cell
 - (iii) Perform a cumulative sum of particle counts
 2. Assign a colour to each cell, in such a way that neighbouring cells have different colours; then, for each colour:
 - (a) Perform a `for_each` on cells
 - (b) Call kernels (6) or (8)

In this way we would iterate on the vector holding the list of particles in each cell, and then inside each cell we would perform only a small amount of serial operations, without any data race.

- On the High Performance Computing side, avenues of development include the porting of the existing code to different backends, such as HIP and ROCm, the support of multi-GPU and multi-node architectures via MPI, and a grid-particles adaptive refinement through a quad-tree approach [47, 13]. Moreover, currently the code employs Structure-of-Arrays for the memory, since, differently from arrays of arbitrary structures, it provides coalescing, which improves memory efficiency [27]. However, recent developments on GPUs computing literature [54, 20] show that the best performance is achieved by adopting an Array of SoA (AoSoA). When addressing the MPI-based multi-GPU implementation, this possibility could

be explored: indeed, the current data structure gives a conceptually straightforward extension towards multi-GPU implementations, where a further level of parallelisation through an MPI-based domain decomposition will make each GPU hold a SoA as the current one, globally giving rise to an AoSoA data structure.

Acknowledgements

Research was sponsored by the Leonardo Labs, Leonardo S.p.A., through the PhD scholarship “Multi-GPUs based PIC / MPM methods for Compressible Flows” funded at Politecnico di Milano and by ICSC - Centro Nazionale di Ricerca in High Performance Computing, Big Data, and Quantum Computing funded by European Union - NextGenerationEU. Views and conclusions contained in this document are those of the author and should not be interpreted as representing the official policies, either expressed or implied, of Leonardo Labs or ICSC.

Conflict of interest

The authors declare that they have no conflict of interest.

References

- [1] Andersen, S., Andersen, L.: Modelling of landslides with the material-point method. *Computational Geosciences* **14**(1), 137–147 (2010)
- [2] Baioni, P.J., Benacchio, T., Capone, L., de Falco, C.: GPUs based material point method for compressible flows. *VIII International Conference on Particle-Based Methods* pp. 1–12 (2023)
- [3] Bardenhagen, S., Brackbill, J., Sulsky, D.: The material-point method for granular materials. *Computer Methods in Applied Mechanics and Engineering* **187**(3), 529–541 (2000)
- [4] Bardenhagen, S.G., Kober, E.M.: The generalized interpolation material point method. *Computer Modeling in Engineering & Sciences* **5**(6), 477–496 (2004)
- [5] Berzins, M.: Energy conservation and accuracy of some MPM formulations. *Computational Particle Mechanics* **9**(6), 1205–1217 (2022)

- [6] Brachet, M.E., Meiron, D.I., Orszag, S.A., Nickel, B.G., Morf, R.H., Frisch, U.: Small-scale structure of the Taylor–Green vortex. *Journal of Fluid Mechanics* **130**, 411–452 (1983)
- [7] Brackbill, J., Ruppel, H.: FLIP: A method for adaptively zoned, particle-in-cell calculations of fluid flows in two dimensions. *Journal of Computational Physics* **65**(2), 314–343 (1986)
- [8] Breyer, M., Van Craen, A., Pflüger, D.: A comparison of SYCL, OpenCL, CUDA, and OpenMP for massively parallel support vector machine classification on multi-vendor hardware. In: *International Workshop on OpenCL, IWOCL’22*. Association for Computing Machinery, New York, NY, USA (2022)
- [9] Bruchon, J., Dignonnet, H., Coupez, T.: Using a signed distance function for the simulation of metal forming processes: Formulation of the contact condition and mesh adaptation. from a Lagrangian approach to an Eulerian approach. *International Journal for Numerical Methods in Engineering* **78**(8), 980–1008 (2009)
- [10] Bull, J.R., Jameson, A.: Simulation of the Taylor–Green vortex using high-order flux reconstruction schemes. *AIAA Journal* **53**(9), 2750–2761 (2015)
- [11] Cao, Y., Chen, Y., Li, M., Yang, Y., Zhang, X., Aanjaneya, M., Jiang, C.: An efficient B-spline Lagrangian/Eulerian method for compressible flow, shock waves, and fracturing solids. *ACM Trans. Graph.* **41**(5), 1–13 (2022)
- [12] Chen, Z., Brannon, R.M.: An evaluation of the material point method. Sandia National Lab. Technical Report (2002). URL <https://www.osti.gov/biblio/793336>
- [13] Cheon, Y.J., Kim, H.G.: An adaptive material point method coupled with a phase-field fracture model for brittle materials. *International Journal for Numerical Methods in Engineering* **120**(8), 987–1010 (2019)
- [14] Clayton, B., Guermont, J.L., Maier, M., Popov, B., Tovar, E.J.: Robust second-order approximation of the compressible Euler equations with an arbitrary equation of state. *Journal of Computational Physics* **478**, 111926 (2023)
- [15] Coombs, W.M., Charlton, T.J., Cortis, M., Augarde, C.E.: Overcoming volumetric locking in material point methods. *Computer Methods in Applied Mechanics and Engineering* **333**, 1–21 (2018)

- [16] de Vaucorbeil, A., Nguyen, V.P., Hutchinson, C.R.: A total-Lagrangian Material Point Method for solid mechanics problems involving large deformations. *Computer Methods in Applied Mechanics and Engineering* **360**, 112783 (2020)
- [17] de Vaucorbeil, A., Nguyen, V.P., Sinaie, S., Wu, J.Y.: Chapter two - Material point method after 25 years: Theory, implementation, and applications. In: S.P. Bordas, D.S. Balint (eds.) *Advances in Applied Mechanics*, vol. 53, pp. 185–398. Elsevier (2020)
- [18] Dyke, M.V.: *An Album of Fluid Motion*. ParabolicPress, Inc. (2008)
- [19] Elafrou, A., Larkin, J.: No More Porting: GPU Computing with Standard C++ and Fortran. NVIDIA - GTC Spring 2023 (2023). URL <https://www.nvidia.com/en-us/on-demand/session/gtcspring23-s51043/>
- [20] Fei, Y., Huang, Y., Gao, M.: Principles towards real-time simulation of material point method on modern GPUs. *arXiv preprint* (2021). URL <https://arxiv.org/abs/2111.00699>
- [21] Fu, C., Guo, Q., Gast, T., Jiang, C., Teran, J.: A polynomial Particle-in-Cell method. *ACM Trans. Graph.* **36**(6), 1–12 (2017)
- [22] Gao, M., Wang, X., Wu, K., Pradhana, A., Sifakis, E., Yuksel, C., Jiang, C.: GPU optimization of material point methods. *ACM Trans. Graph.* **37**(6), 1–12 (2018)
- [23] Goktekin, T.G., Bargteil, A.W., O’Brien, J.F.: A method for animating viscoelastic fluids. *ACM Trans. Graph.* **23**(3), 463–468 (2004)
- [24] Guermond, J.L., Nazarov, M., Popov, B., Tomas, I.: Second-order invariant domain preserving approximation of the Euler equations using convex limiting. *SIAM Journal on Scientific Computing* **40**(5), A3211–A3239 (2018)
- [25] Hariri, F., Tran, T., Jocksch, A., Lanti, E., Progsch, J., Messmer, P., Brunner, S., Gheller, C., Villard, L.: A portable platform for accelerated PIC codes and its application to GPUs using OpenACC. *Computer Physics Communications* **207**, 69–82 (2016)
- [26] Harlow F. H.; Evans, M.W., Harris Jr., D.E.: The Particle-in-Cell method for two-dimensional hydrodynamic problems. Report LAMS-2082 of the Los Alamos Scientific Laboratory (1956)

- [27] Hoberock, J.: Thrust by example: Advanced features and techniques. In: GPU Technology Conference. NVIDIA (2010)
- [28] Hu, Y., Fang, Y., Ge, Z., Qu, Z., Zhu, Y., Pradhana, A., Jiang, C.: A moving least squares material point method with displacement discontinuity and two-way rigid body coupling. *ACM Transactions on Graphics* **37**(4), 1–14 (2018)
- [29] Jiang, C.: The material point method for the physics-based simulation of solids and fluid. Ph.D. thesis, University of California, Los Angeles (2015)
- [30] Jiang, C., Schroeder, C., Teran, J.: An angular momentum conserving affine-particle-in-cell method. *Journal of Computational Physics* **338**, 137–164 (2017)
- [31] Kraus, M., Kormann, K., Morrison, P.J., Sonnendrücker, E.: GEMPIC: geometric electromagnetic particle-in-cell methods. *Journal of Plasma Physics* **83**(4), 905830401 (2017)
- [32] Laskowski, G., Kopriva, J., Michelassi, V., Shankaran, S., Paliath, U., Bhaskaran, R., Wang, Q., Talnikar, C., Wang, Z., Jia, F.: Future directions of high fidelity CFD for aerothermal turbomachinery analysis and design. 46th AIAA Fluid Dynamics Conference (2016)
- [33] Maier, M., Kronbichler, M.: Efficient parallel 3d computation of the compressible Euler equations with an invariant-domain preserving second-order finite-element scheme. *ACM Trans. Parallel Comput.* **8**(3), 1–30 (2021)
- [34] Moutsanidis, G., Long, C.C., Bazilevs, Y.: IGA-MPM: The isogeometric material point method. *Computer Methods in Applied Mechanics and Engineering* **372**, 113346 (2020)
- [35] NVIDIA: CUDA C++ programming guide (2022). URL <https://docs.nvidia.com/cuda/cuda-c-programming-guide/index.html>
- [36] NVIDIA: NVIDIA A100 Tensor Core GPU architecture (2022). URL <https://resources.nvidia.com/en-us-genomics-ep/ampere-architecture-white-paper?xs=169656>
- [37] NVIDIA: Hpc compilers - c++ parallel algorithm (2023). URL <https://docs.nvidia.com/hpc-sdk/compilers/c++-parallel-algorithms/index.html>
- [38] NVIDIA: Thrust release 12.3 (2023). URL <https://docs.nvidia.com/>
- [39] Sadeghirad, A., Brannon, R.M., Burghardt, J.: A convected particle domain interpolation technique to extend applicability

- of the material point method for problems involving massive deformations. *International Journal for Numerical Methods in Engineering* **86**(12), 1435–1456 (2011)
- [40] Samet, H.: The quadtree and related hierarchical data structures. *ACM Computing Surveys* **16**(2), 187–260 (1984)
 - [41] Sod, G.A.: A Survey of Several Finite Difference Methods for Systems of Nonlinear Hyperbolic Conservation Laws. *Journal of Computational Physics* **27**(1), 1–31 (1978)
 - [42] Steffen, M., Kirby, R.M., Berzins, M.: Analysis and reduction of quadrature errors in the material point method (MPM). *International Journal for Numerical Methods in Engineering* **76**(6), 922–948 (2008)
 - [43] Stomakhin, A., Schroeder, C., Jiang, C., Chai, L., Teran, J., Selle, A.: Augmented MPM for phase-change and varied materials. *ACM Transactions on Graphics* **33**(4), 1–11 (2014)
 - [44] Su, Y.C., Tao, J., Jiang, S., Chen, Z., Lu, J.M.: Study on the fully coupled thermodynamic fluid–structure interaction with the material point method. *Computational Particle Mechanics* **7**(2), 225–240 (2020)
 - [45] Sulsky, D., Chen, Z., Schreyer, H.: A particle method for history-dependent materials. *Computer Methods in Applied Mechanics and Engineering* **118**(1-2), 179–196 (1994)
 - [46] Sulsky, D., Gong, M.: Improving the Material-Point Method, pp. 217–240. Springer International Publishing, Cham (2016)
 - [47] Tan, H., Nairn, J.A.: Hierarchical, adaptive, material point method for dynamic energy release rate calculations. *Computer Methods in Applied Mechanics and Engineering* **191**(19), 2123–2137 (2002)
 - [48] Taylor, G.I., Green, A.E.: Mechanism of the production of small eddies from large ones. *Proceedings of the Royal Society of London. Series A - Mathematical and Physical Sciences* **158**(895), 499–521 (1937)
 - [49] Tielen, R., Wobbes, E., Möller, M., Beuth, L.: A high order material point method. *Procedia Engineering* **175**, 265–272 (2017). *Proceedings of the 1st International Conference on the Material Point Method (MPM 2017)*
 - [50] Toro, E.F.: *Riemann Solvers and Numerical Methods for Fluid Dynamics*. Springer (2009)
 - [51] Tran, L.T., Kim, J., Berzins, M.: Solving time-dependent PDEs using the material point method, a case study from gas

- dynamics. *International Journal for Numerical Methods in Fluids* **62**(7), 709–732 (2010)
- [52] Tran, Q.A., Sołowski, W.: Generalized interpolation material point method modelling of large deformation problems including strain-rate effects – application to penetration and progressive failure problems. *Computers and Geotechnics* **106**, 249–265 (2019)
 - [53] Wang, S., Ding, M., Gast, T.F., Zhu, L., Gagniere, S., Jiang, C., Teran, J.M.: Simulation and visualization of ductile fracture with the Material Point Method. *Proc. ACM Comput. Graph. Interact. Tech.* **2**(2), 1–20 (2019)
 - [54] Wang, X., Qiu, Y., Slattery, S.R., Fang, Y., Li, M., Zhu, S.C., Zhu, Y., Tang, M., Manocha, D., Jiang, C.: A massively parallel and scalable multi-GPU material point method. *ACM Trans. Graph.* **39**(4), 1–15 (2020)
 - [55] Wobbes, E., Möller, M., Galavi, V., Vuik, C.: Conservative Taylor least squares reconstruction with application to material point methods. *International Journal for Numerical Methods in Engineering* **117**(3), 271–290 (2019)
 - [56] X. Zhang Z. Chen, Y.L.: *The Material Point Method*. Academic Press, Elsevier (2017)
 - [57] York, A.: Development of modifications to the material point method for the simulation of thin membranes, compressible fluids, and their interactions. Ph.D. thesis, University of New Mexico (1997)
 - [58] York, A.R., Sulsky, D., Schreyer, H.L.: Fluid–membrane interaction based on the material point method. *International Journal for Numerical Methods in Engineering* **48**, 901–924 (2000)